Draft version May 7, 2012
Preprint typeset using LaTeX style emulateapj v. 5/2/11

IMAGING THE ALGOL TRIPLE SYSTEM IN H BAND WITH THE CHARA INTERFEROMETER

F. Baron[1], J. D. Monnier[1], E. Pedretti[2], M. Zhao[3], G. Schaefer[4], R. Parks[5], X. Che[1], N. Thureau[6], T. A. ten Brummelaar[4], H.A. McAlister[4,5], S.T. Ridgway[7], C. Farrington[4], J. Sturmann[4], L. Sturmann[4] and N. Turner[4]

[1]Department of Astronomy, University of Michigan, 918 Dennison Building, Ann Arbor, MI 48109-1090, USA
[2]European South Observatory, Karl-Schwarzschild-Str. 2, 85748 Garching bei München, Germany
[3]Department of Astronomy, Penn State University, 420 Davey Lab State College, PA 16803, USA
[4]The CHARA Array of Georgia State University, Mount Wilson CA 91023, USA
[5]Department of Physics and Astronomy, Georgia State University, Atlanta, GA 30302-3965, USA
[6]Department of Physics and Astronomy, University of St. Andrews, UK and
[7]National Optical Astronomy Observatory, Tucson, AZ 85726-6732, USA

Draft version May 7, 2012

ABSTRACT

Algol (β Per) is an extensively studied hierarchical triple system whose inner pair is a prototype semi-detached binary with mass transfer occurring from the sub-giant secondary to the main-sequence primary. We present here the results of our Algol observations made between 2006 and 2010 at the CHARA interferometer with the Michigan Infrared Combiner in the H band. The use of four telescopes with long baselines allows us to achieve better than 0.5 mas resolution and to unambiguously resolve the three stars. The inner and outer orbital elements, as well as the angular sizes and mass ratios for the three components are determined independently from previous studies. We report a significantly improved orbit for the inner stellar pair with the consequence of a 15% change in the primary mass compared to previous studies. We also determine the mutual inclination of the orbits to be much closer to perpendicularity than previously established. State-of-the-art image reconstruction algorithms are used to image the full triple system. In particular an image sequence of 55 distinct phases of the inner pair orbit is reconstructed, clearly showing the Roche-lobe-filling secondary revolving around the primary, with several epochs corresponding to the primary and secondary eclipses.

Subject headings: binaries:eclipsing - infrared:stars - stars: imaging - stars: individual (Algol, Bet Per, HD 19356) - techniques: interferometric - techniques: image processing - *Online-only material*: animation, color figures

1. INTRODUCTION

Algol (β Per, HD 19356) is one of the most extensively studied stellar systems in the history of astronomy. It is a triple hierarchical system where an inner eclipsing binary is orbited by a more distant outer star. The inner system of orbital period 2.87 days is a prototypical semi-detached binary in nearly circular orbit. The primary, Algol A, is a main-sequence star of type B8V. The secondary, Algol B, is a subgiant of type K2IV. As Algol A and Algol B are thought to have formed roughly at the same time, one would expect the more massive star of the pair to become a subgiant first. However this supposition is contradicted by all observations, showing Algol B to be lighter than Algol A. The solution to this so called "Algol paradox" is that most of the original mass from Algol B, which fills its Roche lobe, is thought to have been accreted by Algol A. As the inner pair is tidally locked, this creates a strong magnetic dynamo effect and non-thermal emission observed in X-ray and radio. Using radio interferometry, Lestrade et al. (1993) detected positional displacement during the orbital revolution of the inner pair and identified Algol B as the source of radio emission. In X-rays, giant flares have been detected on Algol B (White et al. 1986; Schmitt & Favata 1998; Schmitt et al. 2003). Their sizes were estimated to a few tenths of the Algol B radius, and they were shown to follow active and quiescent periodic cycles of 49 days (Richards et al. 2003). Hα profiles provide evidence for mass transfer through a stream of gas from the Roche lobe of Algol B to Algol A (Gillet et al. 1989). In parallel, observations with *EXOSAT* (Favata et al. 2000), *XMM* (Schmitt & Ness 2004) and *Chandra* (Drake 2003) have shown evidence of an extended corona around Algol B. The presence of a large, permanent coronal loop around Algol B, oriented toward Algol A, has very recently been confirmed by radio images from the HSA (Peterson et al. 2010).

The tertiary component, Algol C, was first discovered by radial velocity measurement (Curtiss 1908) and revolves around the inner pair over a period of about 680 days without eclipsing. It is an Am star with metal and hydrogen lines presenting F1V characteristics (Richards 1993). Earlier studies based on astrometric, photometric, and radial velocity data allowed the determination of the masses of the inner stars (Hill et al. 1971; Tomkin & Lambert 1978) and of Algol C (Bachmann & Hershey 1975). Then light curve meta-analyses combining previous visible, infrared and ultraviolet observations (Soderhjelm 1980; Richards & Mochnacki 1988) produced estimates of the orbital elements for the inner and outer orbits, as well as for the surface temperatures, $\log g$, radii and masses of the three stars. With the advent of speckle interferometry, it became possible to spatially resolve the outer component (Labeyrie et al. 1974; McAlister & Degioia 1979), leading to the determination of orbital parameters for the outer orbit (Bonneau 1979). Optical interferometry then improved upon these results with the Mark

fbaron@umich.edu

III interferometer (Pan et al. 1993). However, due to 180° ambiguities in early speckle observations, all studies based on speckle results (Bonneau 1979; Soderhjelm 1980; Pan et al. 1993) produced ascending node estimates for the inner or outer orbits in disagreement with the polarimetric (Rudy & Kemp 1978) and radio (Lestrade et al. 1993) observations. Therefore, as for given inclinations, the angle between the inner and outer orbits solely depends on the difference of the ascending nodes, this ambiguity implied that the orbits were found either roughly perpendicular or coplanar. As coplanarity was ruled out by the shallow eclipse depth of photometric observations (Soderhjelm 1980), ad-hoc corrections had to be made to the ascending nodes of speckle-based studies. More recently, Csizmadia et al. (2009) resolved the inner pair with long baseline interferometry at the Center for High Angular Resolution Astronomy (CHARA), using the CLASSIC instrument working in the near infrared K_s band, in combination with *Very Long Baseline Interferometer* radio observations. They determined the orbit of the inner binary to be in prograde rotation, in disagreement with the retrograde movement found previously in radio by Lestrade et al. (1993). Zavala et al. (2010) recently solved these long-standing issues, by simultaneously resolving all three stellar components in the optical with the Navy Optical Interferometer (NOI). Using angular referencing, the most precise inner and outer orbits to date were derived, with positional errors on the stellar components of the order of a milliarcsecond. The outer orbit was shown to be prograde and the inner orbit retrograde. The latest *Very Long Baseline Array* radio measurements are in agreement with this orientation (Peterson et al. 2011). Zavala et al. (2010) also presented the first reconstructed interferometric image of all three stars, though the short baseline lengths used at NOI precluded full separation of the inner pair components.

In this paper, we present the results of our Algol observations with the Michigan InfraRed Combiner (MIRC) in the H band, making use of the long baselines available at CHARA. In Section 3, the relative positions of the three components are determined by model-fitting for the 55 epochs of our data set. New estimates of the orbital parameters are then derived in Section 4 using these stellar positions. Finally, images of the inner orbit are reconstructed for each epoch in Section 5, where we discuss the potential evidence for the phenomena detected by radio and X-ray instruments.

2. OBSERVATIONS AND DATA REDUCTION

Our observations of Algol were conducted between 2006 and 2010 at the Georgia State University CHARA Array interferometer using the MIRC instrument. The CHARA Array, located on Mount Wilson, CA, consists of six 1 m telescopes and is the largest optical/IR interferometer array in the world (ten Brummelaar et al. 2005). Its 15 baselines range from 34 m to 331 m, providing resolutions up to ~ 0.5 mas at H band and ~ 0.7 mas at K band. Thus the data collected constitute the highest angular resolution data available to date on Algol. MIRC was used to combine four CHARA telescopes together for true interferometric imaging in H band, providing six visibilities, four closure phases and four triple amplitudes simultaneously in eight narrow spectral bands for each snapshot (Monnier et al. 2006).

Our observations total 20 nights, making the accumulated interferometric data on Algol one of the largest datasets to date at CHARA. In particular, the data covers most phases of the inner pair eclipse. A complete observing log is listed in Table 1, including our calibrators. The spacing of Algol observations is not regular: Algol was sometimes observed only as a backup target, when atmospheric conditions did not allow for other fainter targets. The duration of most of these observations generally did not exceed 1 h. Two array configurations were used, S1-E1-W1-W2 and S2-E2-W1-W2. The full complement of fringes was always obtained except on 2009 August 18 when bad seeing prevented the acquisition of the E1 fringes. Both configurations are well-adapted to imaging, with roughly equal Fourier coverage in all directions. Figure 1 presents the typical Fourier coverage achieved within one of our final data sets.

The standard observing procedures were followed, and the data were reduced using the standard MIRC pipeline described in Monnier et al. (2007). After frame coadding, background subtraction and a Fourier transform of the raw data, fringe amplitudes and phases are used to form squared-visibilities and triple products. On all data prior to 2010, the photometric calibrations are estimated using shutter matrix measurements and partial beam chopping. Starting in 2010 data, the calibration relies on the newly available (and far superior) photometric channel technique, allowing flux measurement in parallel with the fringes (Che et al. 2010). During the next step, calibrators are used to calibrate the drifts in overall system response. Table 2 presents the sizes of the calibrators, as estimated from our ongoing study of "good" interferometric calibrators and based on three independent photometry methods, adopting different color–magnitude relations to compute the stellar sizes. It has to be noted here that 37 And is currently suspected to be a binary, though with a flux ratio between components large enough not to significantly affect the calibration. After calibration, the pipeline outputs the final calibrated power spectra and bispectra into files compliant with the OIFITS standard (Pauls et al. 2005).

Based on the orbital parameters obtained by previous studies, we expect significant stellar movement on short timescales. The orbital period of the inner pair is about 2.87 days, meaning that Algol B is moving relatively to Algol A by about 0.07 mas in an hour. The movement of Algol C also impacts the visibilities through high order lobes which oscillate rapidly with its separation from the inner pair (ranging from 15 to 70 mas), though this phenomenon is somewhat mitigated by its much longer orbital period (about 680 days).

While model-fitting can possibly be made to account for these time dependencies, image reconstruction packages currently cannot. At best, an image reconstructed using our data accumulated over an hour would be blurred, and at worse it would not converge at all toward a meaningful solution. Thus, the data have to be split into shorter sequences of no more than 10 minutes, finding a compromise between reasonable Fourier coverage and temporal consistency. This splitting is applied to about 60% of the nights and results in a total of 55 different files, each of which contains about 240 power spectra and 160 bispectra, sufficient for imaging without

blurring. Figures 2 and 3 illustrate how the data accumulated on 2009 August 12 have been split into chunks.

3. MODEL FITTING

The purpose of model-fitting here is to derive the position, shape and flux parameters of all three Algol components. These parameters will then be used to determine the orbital parameters of the inner orbit (noted A–B) and outer orbit (noted AB–C), as well as to generate realistic prior images for later image reconstruction. Our general procedure is to minimize the residuals between the interferometric observables derived from our current model and the corresponding interferometric data, using a Levenberg-Marquardt algorithm. Two possible paths were initially examined: either directly fit the orbital parameters on the full data set, or estimate a separate set of parameters for every single epoch and then fit the orbital parameters using these positions. As Algol B is non-spherical (because it is thought to fill its Roche lobe), the two-dimensional projection of its surface onto the observing plane varies from night to night (Richards 1992). The "global fit" approach would require a complex three–dimensional model of the three stars, while the "night-to-night fit" approach we finally settled for is more flexible, as well as more manageable in terms of computing power and memory requirements.

Each star is modeled here as an ellipse of uniform brightness distribution. As the angular sizes of the components are only few times the array resolution, the use of limb-darkening coefficients would have a nearly negligible impact on the visibilities. In fact, limb-darkened models are not strictly necessary for orbit fitting and even detrimental as they increase the number of parameters to estimate. Furthermore we expect image reconstruction to retrieve the true flux distribution. A major effect to take into account when modeling the system is the bandwidth smearing effect on Algol C, i.e. Algol C's contribution to the visibilities is affected by its large separation from the delay-tracking center (Algol A) and the width of each of the MIRC spectral channels. With this effect, the total number of parameters to estimate for each epoch is 23: the principal axes and angles for Algol B and Algol C relative to Algol A (the available interferometric data does not give access to absolute positions), the relative flux contributions of Algol A and Algol B to the total flux (normalized to unity), the shape parameters of the three elliptical disks (semimajor axis, ellipticity, and angular orientation), and the bandwidth smearing factors for Algol C (one for each spectral channel).

The χ^2 formed from power spectra and bispectra is known to be multimodal: as the Levenberg–Marquardt is a gradient algorithm, the parameters have to be initialized close to their true value to prevent falling into local minima. Attempting to estimate the 23 unknowns simultaneously would only lead to inconsistent results. We determined that the positions of Algol B and Algol C relative to Algol A constitute the parameters with the most influence on the χ^2. Therefore our solution to this convergence problem involves simultaneous systematic grid searches on both Algol B and Algol C Cartesian coordinates (relative to Algol A), coupled to Levenberg-Marquardt optimizations on the remaining parameters. In addition, some parameters can safely be fixed, based on the literature of the expected physical properties of the system. As Algol A and B are thought to be tidally locked (Richards 1992), the inner orbit is posed circular. The principal axis of Algol B is supposed to be along the direction A-B, as expected for a Roche-lobe filling secondary. Algol A and Algol C are both assumed perfectly circular, because they are not rapid rotators and are not filling their Roche lobes. With these assumptions the χ^2 fit on the remaining number of parameters is then well constrained as each data set contains between 120 and 240 power spectra as well as between 60 and 160 bispectra (triple amplitudes and closure phases). Out of the eclipse periods, lower and higher bounds are imposed on each parameter solely to enforce the physical meaning of parameters. During the eclipses, the aspect ratios of Algol B are kept small (< 1.05).

The fitting is done in two steps – first a coarse grid search on Algol B and Algol C positions, then a finer one. The coarse search uses a 10×10 grid with spacing 0.1 mas aimed at determining the approximate positions of the components. For each epoch, the center of the Algol C grid is initialized at its expected position based on the orbital elements from the NOI results (Zavala et al. 2010), while the center of the Algol B grid search is simply set to the origin $(0, 0)$ (i.e., Algol A position). For a given night, this setup of the coarse grid search covers all the probable positions of the components. Then the finer grid search refines the estimates, using a 10×10 grid with spacing 0.02 mas around the most likely positions found during the coarse search. To insure convergence during both the coarse and fine searches, the fluxes and angular diameters of the star are always optimized first, while the secondary ellipticity and the bandwidth smearing factors are kept fixed to their initial estimates; then the constraints on these are relaxed and all parameters are re-optimized.

To compute the visibility contribution of Algol C, an analytic expression of the complex visibilities of a bandwidth-smeared ellipse is directly employed. For the visibility contribution of the inner pair, the presence of epochs where one component eclipses the other prevents the use of analytic expressions. Algol A and Algol B are therefore modeled as ellipses on an image array of 64 by 64 pixels with a pixel size of 0.05 mas. To prevent problems linked to the discretization of the ellipse sizes with this pixellation, the edges of the ellipses are smoothed by a sigmoid function, so that the χ^2 varies continuously with the size parameters. The complex visibilities are then computed by applying a Discrete Fourier Transform to the image. Finally the model power spectra and bispectra are derived from the visibilities, and the reduced χ^2 is computed.

Table 3 reports these reduced χ^2 values for every night. Typically the agreement between the model and the data is good, especially considering the unrealistic assumption of uniform brightnesses: the values lie mostly within the 1.0–6.0 range, with higher χ^2 values encountered during the eclipse epochs where this model breaks down. Figure 4 presents the residuals of a typical fit, which show no noticeable trend.

The full output of our model-fitting software consists in reduced χ^2 maps as a function of Algol B and Algol C positions, as presented on Figure 5. The most probable positions of Algol B and Algol C correspond to the peak value of these maps. For each map, the contour at 1σ

(68% confidence level) is computed and fitted by an ellipse. The positions of the peaks for Algol B and Algol C as well as the parameters of the error ellipses (major and minor axes, angles) are recorded in Table 3.

The fits also produce estimates for the angular diameters of all three stars. The estimates are $\phi_A = 0.88 \pm 0.05$ mas, $\phi_B = 1.12 \pm 0.07$ mas, and $\phi_C = 0.56 \pm 0.10$ mas. For Algol B, this angular diameter corresponds to the major axis of the ellipse (the aspect ratio of the Algol B ellipse changes with the phase of the inner orbit, between 1.04 and 1.22 for our data sets, which we attribute the projection of the Roche lobe).

Concerning Algol C, we note that the difficulty of estimating the bandwidth smearing factors is reflected here as a larger error bar associated with its angular diameter. Our angular diameters are not directly comparable with the published values in Table 1 of Zavala et al. (2010), as these suffered from a conversion error (i.e. the parallax values in milliarsceconds and parsecs have been confused). Nevertheless, as they were based on the linear diameters estimated in Richards (1993), we settle for comparison with Richards (1993) only. We will assume the most recent value published for the orbital parallax, 34.7 ± 0.6 mas, independently determined by optical (Zavala et al. 2010) and radio (Peterson et al. 2011) interferometry, and more precise than the latest *Hipparcos* estimate of 36.17 ± 1.40 mas (van Leeuwen 2009). Finally the linear stellar radii computed with this parallax are given in Table 4: our results are consistent with the radius estimates derived by light curve analysis in Richards (1993), though they admittedly have greater error bars due to the night-by-night nature of our fits and the uniform brightness assumption.

4. ORBITAL SOLUTION

Using the estimates of the relative positions of the components established in Section 3, the orbital parameters for the inner and outer orbits are derived.

The orbital elements for both orbits and the mass ratio m_A/m_B are fitted simultaneously, again using the Levenberg–Marquardt algorithm. The parameters are initialized around the published values in Zavala et al. (2010), for which the corresponding reduced χ^2 is about 13.0. After convergence our final best χ^2 is 0.94. In addition to these orbital parameters, Kepler's third law applied to both the inner and outer orbits allows us to derive the mass ratio $m_C/(m_A + m_B)$ independently from parallax assumptions. The parameters corresponding to the best fit are given in Tables 4–6, with error bars corresponding to a 68% confidence level. The probability distributions of the parameters were obtained with the bootstrapping-with-replacement technique (using 50000 bootstrap samples) and thus takes into account correlated errors. In the case where distributions were found to be roughly symmetrical about the peak values, only a single error bar is given. Figures 6 and 7 show, respectively, the inner and outer orbits corresponding to our best fit, as well as the estimated positions of Algol B and Algol C as determined in the previous section.

Most of our estimated orbital elements are in agreement with previous results based on light curve analysis (Richards 1993) and radio and optical interferometry (Zavala et al. 2010; Peterson et al. 2011). In particular the respective prograde and retrograde movements of the outer and inner orbits are unambiguously verified (see also the reconstructed image sequence of the inner orbit in the next section). The mutual inclination angle i_m between both orbits is given by:

$$\cos i_m = \cos i_1 \cos i_2 + \sin i_1 \sin i_2 \cos(\Omega_1 - \Omega_2) \quad (1)$$

where i_1 and i_2 are the inclination of the inner and outer orbits, and Ω_1 and Ω_2 are the associated ascending node angles. The mutual inclination determines the period of orbital precession between the orbits, and consequently the amplitude of the variations of inclination of the close binary due to dynamical effects (Borkovits et al.(2004) Borkovits Forgács-Dajka). Previously published values close to 100° (Kiseleva et al. 1998) would imply a detectable change of inclination of the close binary from 1° to 3° in the last century, which in turn would lead to observable variations in the minimum depth of the light curves of the eclipse and the disappearance of these eclipses after a few centuries (Csizmadia et al. 2009). This is however contrary to the actual observations: Algol eclipses have been known since Antiquity and therefore the minimum depth is not thought to have significantly changed within error bars. The mutual inclination estimate derived from our bootstrap results is $i_m = 90°.20 \pm 0°.32$. It is completely consistent with photometric observations, and much closer to exact perpendicularity than the most recent estimate of $95° \pm 5°$ (Zavala et al. 2010).

The main point of disagreement between previous studies and our work is that we found the semi-major axis of the inner orbit to be slightly smaller, in turn implying a smaller value for the total mass of the inner binary. However, to disregard this shorter axis result we would have to invoke a 15% error in our estimation of the position of the center of mass of the secondary. As our analysis is essentially based on the determination of photocenters, a potential source of error to consider is the asymmetric brightness distribution on the surface of a Roche-lobe-filling star. We quantified the magnitude of such an effect, by simulating the equatorial brightness profile of Algol B, taking into account both gravity darkening and limb darkening as shown in Figure 8. The positions of the photocenter and of the center of mass were found to coincide to 1%. Arguably the existence of an additional strong proximity effect (due to the primary heating of the atmosphere of the secondary) could also explain a photocenter shift. Detailed modeling of such effect however goes beyond the scope of this paper, requiring complementary data (imaging in Section 5 based on current data did not allow detection of the proximity effect). Finally, the semimajor axis of the inner binary was also found to be 15% smaller than previous optical results by recent radio (Peterson et al. 2011) and X-ray observations (Chung et al. 2004), a result strikingly similar to ours. While both these papers hypothesized the existence of a coronal component around Algol B, no coronal signature has been detected in the near-infrared yet. Our result thus suggests the possibility that the center of light and center of mass actually roughly coincide, with previous optical results suffering from imprecisions. Our observations indeed benefited from much higher angular resolution than previous interferometric studies and from the recent disambiguation of the orbital angles from Zavala et al. (2010).

Consequently we recommend that our orbits (like all previously published orbits based on interferometric data) should be interpreted as photocenter orbits. We also note that we did not notice significant differences between the center of lights estimated by model-fitting uniform ellipses and estimated by using the real brightness distribution. In Section 5 we demonstrate that the semimajor axes estimated from the disk model and from the reconstructed images differ by no more than 5%.

The inner binary mass ratio $m_A/m_B = 4.56 \pm 0.34$ agrees with the most recent radial velocity measurements (Hill et al. 1993, 1971; Tomkin & Lambert 1978) which measured $m_A/m_B = 4.6 \pm 0.1$. Our larger error bar is due to the lesser intrinsic precision of interferometry in this parameter, as the mass ratio influences the position of Algol C only by a small amount. Figure 9 shows that the χ^2 of the Algol C orbit fit possesses a very flat minimum valley, resulting in the large error on the mass ratio.

With the assumption of a parallax of 34.7 ± 0.6 mas (Zavala et al. 2010; Peterson et al. 2011), the masses of the three stars are completely determined and we report the results in Table 4. Algol A and Algol B are lighter than found by Zavala et al. (2010) and Richards (1993). We note here that the tertiary mass published in Zavala et al. (2010) is numerically inconsistent with the corresponding semi-axes and periods, which seems to be due to slightly different parallax values adopted for the inner and outer orbit fits (C. Hummel, private communication, 2011). With our hierarchical fit, we find the mass of Algol C to be larger than that published in Richards (1993). Overall our mass estimates are consistent with all measurements (radial velocity and system dynamics) and give a sensibly different view of the system. In particular the picture of the mass transfer within the inner binary may have to be modified.

5. IMAGE RECONSTRUCTION

The amount of data present in each MIRC data sets corresponds to a dozen minutes of observation each night. All data sets except one (2009 August 18) contain four-telescope data. Consequently there is enough phase information to attempt "model-independent image reconstruction" on each night, where the prefix "model-independent" underlines that the method does not rely on a specific astrophysical model.

The image reconstruction procedure belongs to the class of "ill-posed" inverse problems, as it attempts to reconstruct an image conventionally consisting in a large number of pixels (typically a few thousand) using the less numerous interferometric data points (typically a few hundred). Expressing the problem in a Bayesian framework shows that the solution can be given by the regularized maximum likelihood method (Baron et al. 2010; Thiébaut & Giovannelli 2010). The target image is the array of fluxes $\widehat{\boldsymbol{x}} = \{x_0, \dots x_{n-1}\}$ that minimizes the sum of a term linked to the data (the likelihood) and a term reflecting all prior information (the regularization) under the two constraints of image positivity and of normalization of the image to unity, i.e. in the mathematical form:

$$\widehat{\boldsymbol{x}} = \underset{\boldsymbol{x}\in\mathbb{R}^n}{\arg\min} \left\{ \chi^2(\boldsymbol{x}) + \mu R(\boldsymbol{x}) \right\}. \qquad (2)$$

subject to positivity ($\forall i,\ x_i \geq 0$) and normalization ($\sum_{i=0}^{n-1} x_i = 1$). The likelihood term measures the distance between the observed power spectrum and bispectrum and the same quantities derived from the tentative image. Minimizing this term enforces the presence of flux as indicated by the data, but the minimization presents many local minima. The addition of the regularization function $R(\boldsymbol{x})$ discriminates between these local minima, as well as prevents over-fitting, detrimental to image quality. The factor μ in Equation (2) controls the relative weight of the χ^2 and regularization terms, and can be chosen so that the actual reduced χ^2 is roughly unity for the reconstructed image (the selection of the truly optimal μ is a difficult problem which goes beyond the scope of this paper). Most regularizers are computed in the image plane, but also possesses good frequency extrapolation properties in the Fourier plane. Hence they allow reconstructions to routinely achieve super-resolution, i.e., to produce images with an effective resolution typically about four times greater than the physical array resolution.

The image reconstruction software SQUEEZE (Baron et al. 2010) has been used to obtain the reconstruction presented in this paper. It combines the Markov Chain Monte Carlo and gradient-descent approaches used respectively by its predecessors MACIM (Ireland 2006) and BSMEM (Baron & Young 2008). SQUEEZE offers a vast choice of regularizers, ranging from classic entropy to novel wavelet regularizations. As the images of Algol are expected to consist of three compact limb-darkened stars, we choose to use the total variation regularizer, an edge-preserving regularizer which ensures both the smoothness and the compactness of the stars while strongly penalizing stray flux (Rudin et al. 1992). In our implementation, the total variation is implemented as:

$$R_1(\boldsymbol{x}) = \sum_i -\mathrm{TV}(x_i) = \sum_i |x_{i+1} - x_i|, \qquad (3)$$

A second regularizer is also employed in the form of a prior image to initialize the Markov Chain to a sensible starting point as well as to prevent the exploration of pixels where the presence of flux is known to be very improbable. The prior image $\boldsymbol{m}$ is created by convolving the best model image of Section 3 to one fourth of the array resolution. The entropic prior expression is the Burg entropy (Burg 1975):

$$R_2(\boldsymbol{x}) = \sum_i -\log(x_i/m_i). \qquad (4)$$

The number of pixel elements in the Markov Chain is set to 4000, and the length of the Chain to 10000 iterations. A common size and pixellation is chosen for all 55 images to allow easier comparison. The highest instrumental resolution is given by the largest CHARA baseline (S1-W1, 330 m), corresponding to 0.5 mas in the H band. Taking into account the expected amount of super-resolution, our choice of pixellation for the reconstructed images is thus 0.1 mas. Meanwhile the distance from Algol C to the inner pair is at most 100 mas, thus requiring an image size of 1000×1000 pixels. This is a factor 100 more pixels than typical binary reconstructions from non-simulated data in optical/infrared interferometry (Zhao et al. 2008). Nevertheless all 55 reconstructions converged without notable issues, with final

reduced χ^2 between 1.0 and 2.0.

Figure 10 presents the reconstruction for 2009 August 12. The three stars are present within a small field of 16 mas, Algol C being close to its periapsis, and they are well resolved.

Algol A appears as a bright and near-perfect circular disk with a small amount of limb-darkening. Algol B is fainter and elongated toward Algol A, as expected due to it filling its Roche lobe. Algol C also appears elongated in the direction of Algol A–B, though this is only here a purely optical-numerical artifact due to bandwidth smearing.

All the reconstructed images of the inner pair are presented in Figure 11, with epochs sorted by increasing phase of the inner eclipse. A movie generated from this sequence is also available with the online version of this paper. These images should be interpreted with caution, due to the comparatively poor resolution of the interferometer compared to the size of the stars, and to the typically limited dynamic range of image reconstruction with four telescopes (about 10:1). Overall the aspect of Algol A barely changes from image to image, while Algol B's elongation varies as expected with the phase of the eclipse.

Due to the sporadic nature of our Algol observations, the phase coverage is unequal and incomplete, and in particular there are no data available beyond phase 0.861. About 20% of the images correspond to snapshots taken during the eclipse epochs. Images with a phase below 0.08 correspond to the primary eclipse, when Algol A is occulted by Algol B. The progressive separation of the stars is clear as the phase increases up to 0.25 (even though the data for these images were taken several years apart). Images with a phase between 0.45 and 0.55 correspond to the secondary eclipse. During part of the secondary eclipse, Algol B seems to completely disappears behind Algol A despite its larger size, an effect we attribute to its lower brightness and the low dynamic range.

In a significant number of images the secondary is clearly limb brightened, a phenomenon we attribute to gravity darkening. We can neither rule out nor confirm the presence of spots on the stellar surfaces, such as hypothesized in Richards (1990, 1992). Similarly, we are unable to confirm the existence of a stream of matter between the stars or of an active corona around Algol B such as detected in radio (while the 2009 August 18 image at phase 0.463 would seem to show some interesting interaction between the stellar pair, it is the least reliable of all images due to data availability on three telescopes only).

Using our reconstructed images, we can now quantify the impact of our assumption of uniformly bright stars adopted in Section 3. As a function of the inner orbit phase, Figure 12 presents the amount of correction to the principal axis of A–B introduced by using the brightness distributions given by the imaging. No significant trend is detected. The maximum correction is 0.057 mas, roughly corresponding to half a pixel, and thus always within one standard deviation of the positions given in Table 3. Consequently, this validates our modeling in Section 3 and increase our confidence in the derived orbital solution.

6. CONCLUSION

From the analysis of the CHARA/MIRC infrared data on Algol we derived new orbital elements of the triple system with unprecedented precision. The respectively prograde and retrograde nature of the outer and inner orbits is unambiguously confirmed and the mutual inclination of the orbital planes is found to be extremely close to perfect perpendicularity. Our results suggest that the semi-major axis of the inner orbit is shorter than previously reported by other methods. While this effect could in theory be due to a shift of the photocenter with respect to the center of mass, we did not find evidence to support this assumption. If our orbits reflect the center of mass orbit, then the masses of the primary and secondary are found to be lighter than suggested by previous works. Using model-independent image reconstruction techniques, we reconstructed a sequence of 55 images of the inner binary with an effective resolution of 0.2 mas. This "movie" of Algol A and Algol B covers most phases of the inner pair, including the primary and secondary eclipses. While the array resolution did not allow us to confirm the detection of potential flares or spots on the surface of the stars, the Roche-lobe shape of the secondary is clearly visible.

To further improve the orbital solution presented in this paper, three-dimensional and time-dependent image reconstruction algorithms are currently being developed at the University of Michigan. By modeling the secondary as a Roche lobe and by imaging directly on spheroids, we expect to considerably enhance the quality of the reconstructions, enabling us to detect potential surface features on the stars.

We thank Bob Zavala (NOI) and Christian Hummel (ESO) for their constructive criticisms on the manuscript.

We are grateful to the reviewers for directing our attention to the potential effects of the asymmetric brightness distribution on a Roche lobe surface.

The authors acknowledge funding from the NSF through awards AST-0807577 to the University of Michigan.

Operational support for the CHARA Array is provided by the National Science Foundation through grant AST-0908253 and by the College of Arts and Sciences at Georgia State University.

CHARA (MIRC)

REFERENCES

Bachmann, P., & Hershey, J. 1975, AJ, 80, 836
Barnes, T., Evans, D., & Moffett, T. 1978, MNRAS, 183, 285
Baron, F., Monnier, J., & Kloppenborg, B. 2010, Proc. SPIE, Vol. 7734, 77342I
Baron, F., & Young, J. S. 2008, Proc. SPIE, 7013, 70133X
Bonneau, D. 1979, A&A, 80, L11
Bonneau, D., et al. 2006, A&A, 456, 789
Borkovits, T., Forgács-Dajka, E. & Regály, Zs., 2004, A&A, 426, 951
Burg, J. 1975, PhD thesis, Stanford Univ.
Che, X., Monnier, J., & Webster, S. 2010, Proc. SPIE, 7734, 77342V
Chung, S., Drake, J., Kashyap, V., Lin, L., & Ratzlaff, P. 2004, ApJ, 606, 1184
Csizmadia, S., et al. 2009, ApJ, 705, 436

Curtiss, R. 1908, ApJ, 28, 150
Drake, J. J. 2003, ApJ, 594, 496
Favata, F., Micela, G., Reale, F., Sciortino, S., & Schmitt, J. H. M. M. 2000, A&A, 634, 628
Gillet, D., Mouchet, M., & North, P. 1989, A&A, 219, 219
Hill, G., Barnes, J., Hutchings, J., & Pearce, J. 1971, The Astrophysical Journal, 168, 443
Hill, G., Perry, C., & Khalesseh, B. 1993, A&AS, 101, 579
Ireland, M. J. 2006, Proc. SPIE, 6268, 62681T
Kervella, P., Mérand, A., Szabados, L., Fouqué, P., Bersier, D., Pompei, E., & Perrin, G. 2008, A&A, 480, 167
Kiseleva, L. G., Eggleton, P. P., & Mikkola, S. 1998, Monthly Notices of the Royal Astronomical Society, 300, 292
Labeyrie, A., Bonneau, D., Stachnik, R., & Gezari, D. 1974, The Astrophysical Journal, 194, L147
Lestrade, J., Phillips, R., Hodges, M., & Preston, R. 1993, The Astrophysical Journal, 410, 808
McAlister, H., & Degioia, K. 1979, ApJ, 228, 493
Monnier, J., et al. 2006, Proc. SPIE, 6268, 62681P
Monnier, J. D., Zhao, M., Pedretti, E., et al. 2007, Science, 317, 342
Pan, X., Shao, M., & Colavita, M. 1993, ApJ, 413, L129
Pauls, T., Young, J., Cotton, W., & Monnier, J. 2005, PASP, 117, 1255
Peterson, W., Mutel, R., Güdel, M., & Goss, W. 2010, Nature, 463, 207
Peterson, W. M., Mutel, R. L., Lestrade, J.-F., Güdel, M., & Goss, W. M. 2011, ApJ, 737, 104
Richards, M. 1992, ApJ, 387, 329
Richards, M. 1993, ApJS, 86, 255
Richards, M., & Mochnacki, S. 1988, The Astronomical Journal, 96, 326
Richards, M. T. 1990, ApJ, 350, 372
Richards, M. T., Waltman, E. B., Ghigo, F. D., & Richards, D. S. P. 2003, ApJS, 147, 337
Rudin, L., Osher, S., & Fatemi, E. 1992, Phys. D: Nonlinear Phenom., 60, 259
Rudy, R., & Kemp, J. 1978, ApJ, 221, 200
Schmitt, J., & Favata, F. 1998, AJ, 96, 326
Schmitt, J., & Ness, J. 2004, A&A, 415, 1099
Schmitt, J., Ness, J., & Franco, G. 2003, A&A, 412, 849
Soderhjelm, S. 1980, A&A, 89, 100
ten Brummelaar, T., McAlister, H., Ridgway, S., et al. 2005, ApJ, 628, 453
Thiébaut, E., & Giovannelli, J. 2010, Signal Process. Mag. IEEE, 27, 97
Tomkin, J., & Lambert, D. L. 1978, ApJ, 222, 119
van Leeuwen, F. 2009, A&A, 500, 505
White, N., Culhane, J., Parmar, A., et al. 1986, ApJ, 301, 262
Zavala, R., Hummel, C., Boboltz, D., et al. 2010, ApJ, 715, L44
Zhao, M., Gies, D., & Monnier, J. 2008, ApJ, 684, L95

Table 1
Days of observation of Algol with CHARA/MIRC

UT Date	Telescope configuration	Calibrators
2006 Oct 9	S2-E2-W1-W2	Zet Per
2006 Oct 11	S2-E2-W1-W2	Zet Per
2006 Oct 12	S2-E2-W1-W2	Zet Per
2007 Oct 4	S1-E1-W1-W2	37 And, Zet Per
2007 Nov 23	S1-E1-W1-W2	Gam Tri
2008 Aug 18	S1-E1-W1-W2	Zet Per
2008 Aug 19	S1-E1-W1-W2	Zet Per
2008 Aug 20	S1-E1-W1-W2	37 And
2008 Aug 21	S1-E1-W1-W2	37 And, Zet Per
2009 Aug 10	S1-E1-W1-W2	Gam Tri
2009 Aug 11	S1-E1-W1-W2	Gam Tri
2009 Aug 12	S1-E1-W1-W2	Gam Tri
2009 Aug 13	S1-E1-W1-W2	Gam Tri
2009 Aug 18	S1-W1-W2	Gam Tri
2009 Aug 19	S1-E1-W1-W2	Gam Tri
2009 Aug 20	S2-E2-W1-W2	Gam Tri, Zet Per
2009 Aug 21	S2-E2-W1-W2	Gam Tri
2009 Aug 24	S2-E2-W1-W2	37 And
2010 Aug 6	S2-E1-W1-W2	Gam Tri, 10 Aur
2010 Aug 8	S2-E1-W1-W2	Gam Tri, 10 Aur

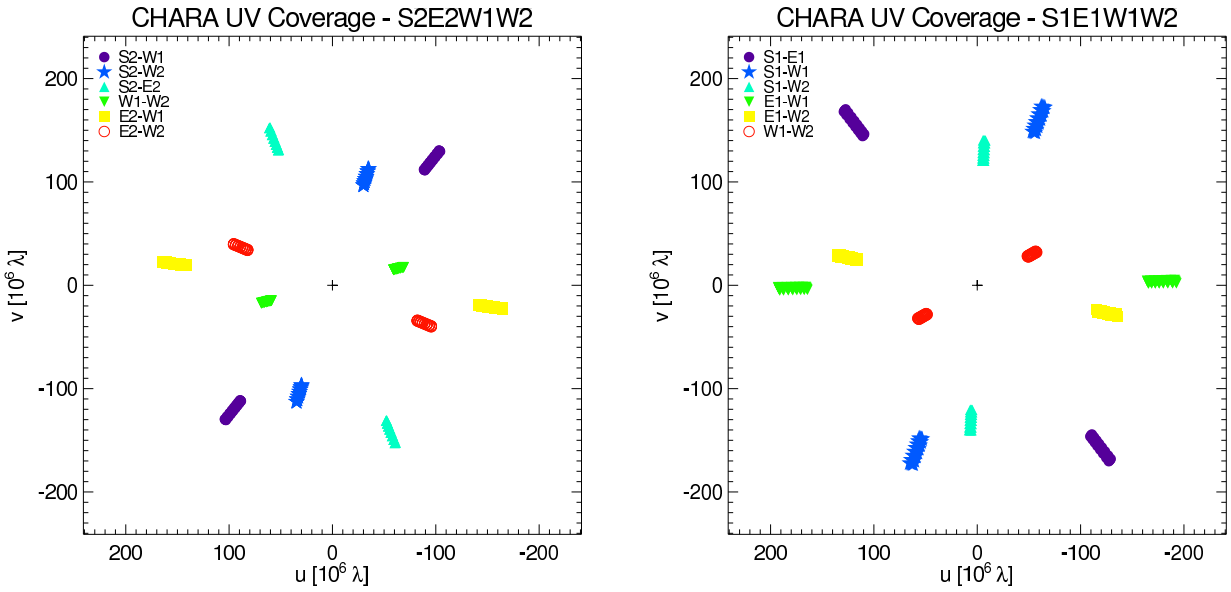

Figure 1. Typical *uv* coverage for one of our Algol "split" data set when using the telescope configuration S2-E2-W1-W2 (left) and S1-E1-W1-W2 (right).

Table 2
Calibrator sizes and 1σ Error in Milli-arcseconds.

Calibrator	Uniform Disk Size (mas)	Error (mas)	Reference
10 Aur	0.419	0.063	b
37 And	0.682	0.030	a,b
Gam Tri	0.522	0.033	a, b, c
Zet Per	0.703	0.021	b

References. — (a) Kervella et al. (2008) ; (b) Barnes et al. (1978) ; (c) Bonneau et al. (2006).

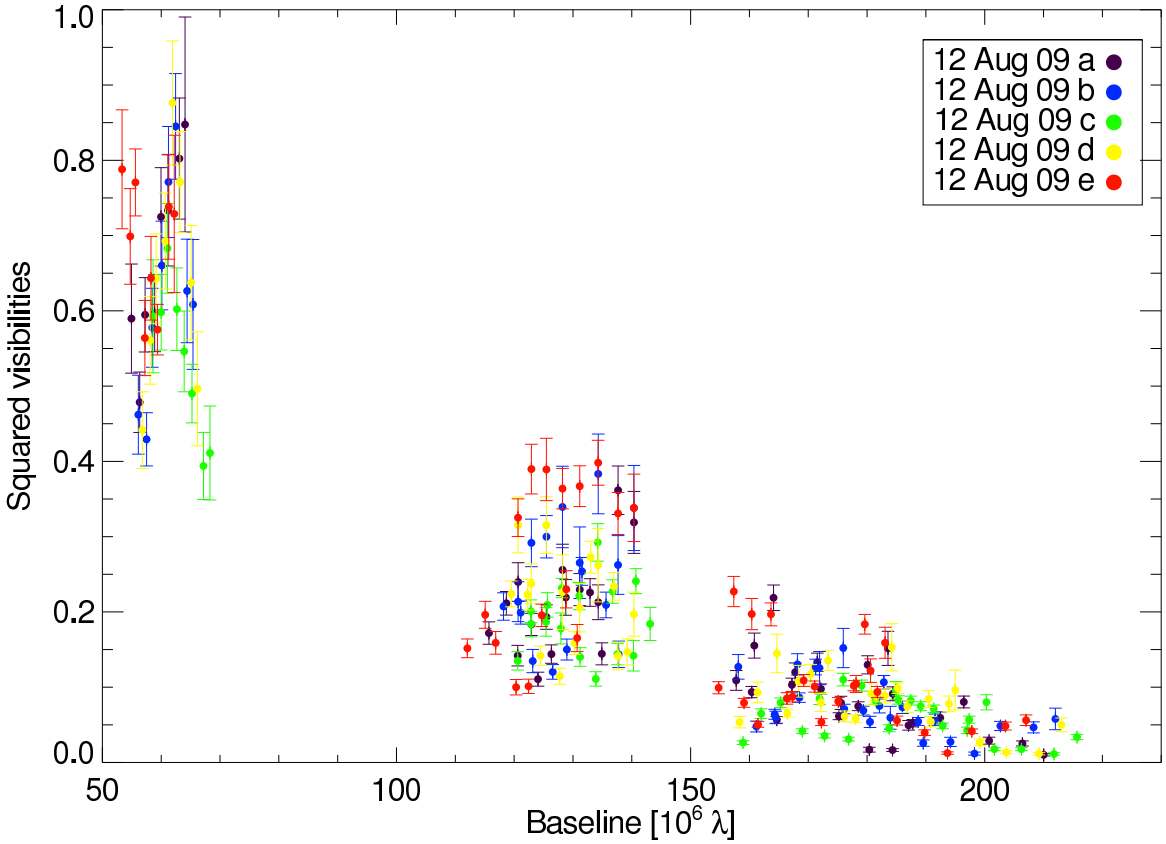

Figure 2. Squared visibilities collected on 2009 August 12, demonstrating how the dataset has been splitted into 5 epochs (2009 August 12 a,b, . . . e). Both Algol visibilities and the *uv* coverage are significantly changing over the course of 20 minutes. For clarity we only show one–fifth of the full data set.

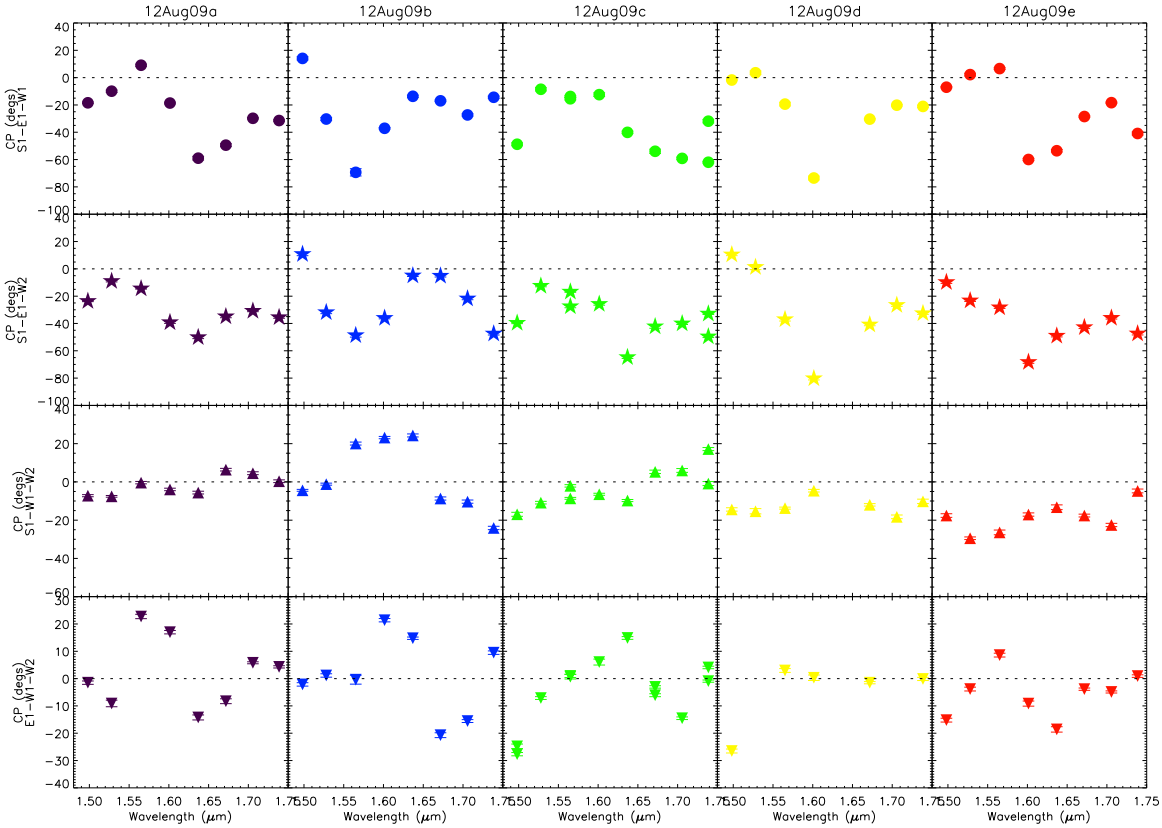

Figure 3. Closure phase data collected on 2009 August 12 presented as a function of wavelength and sorted by epochs. The error bars on the closure phases are of the order of 1°.

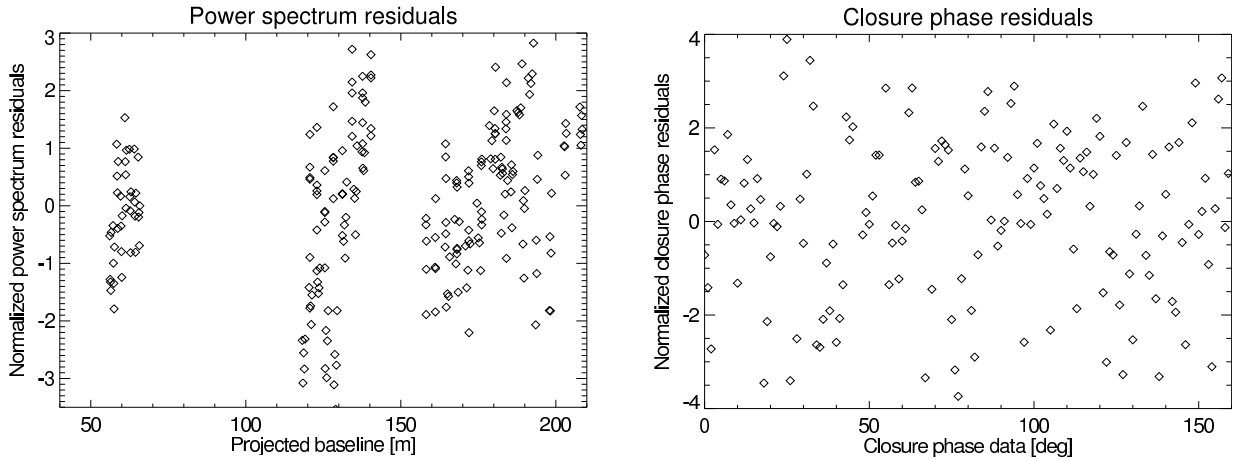

Figure 4. Power spectrum residuals (left) and closure phase residuals (right) normalized by the data error, here for the 2009 August 12 a data set, with a reduced χ^2 of 1.16.

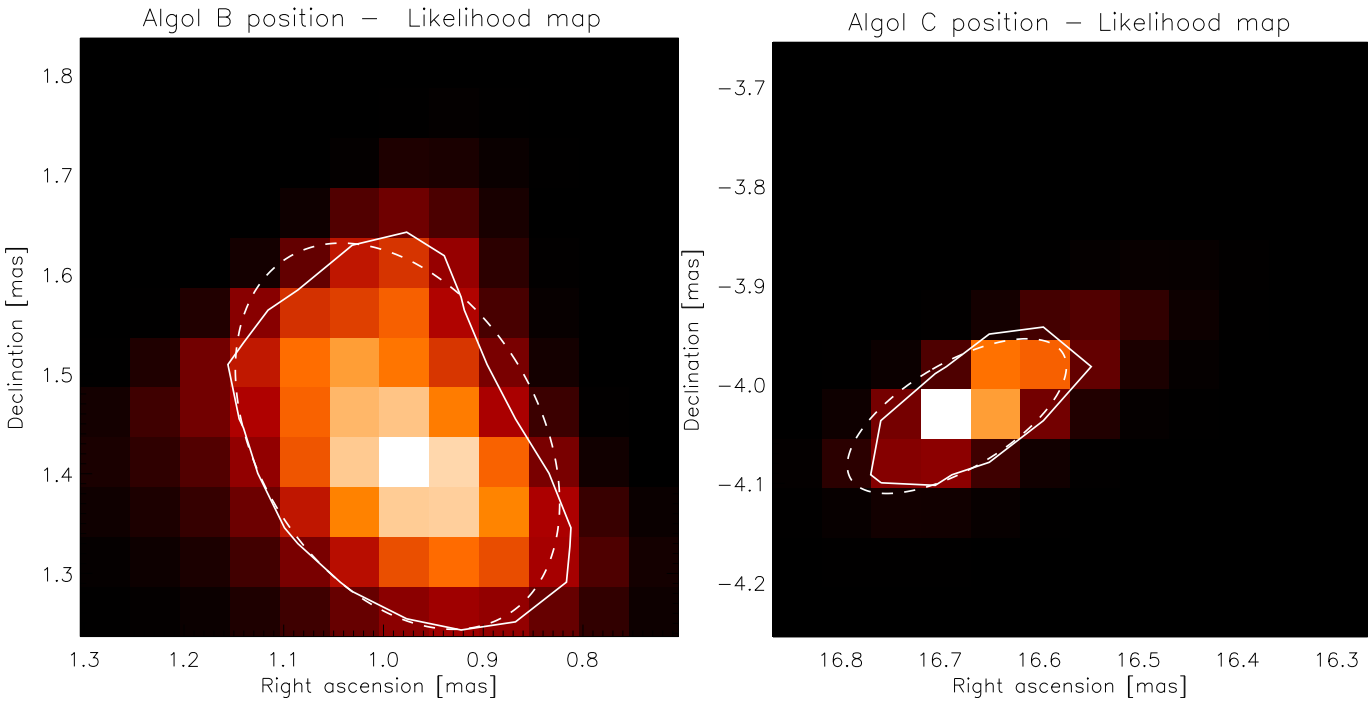

Figure 5. Likelihood maps of Algol B (left) and Algol C (right) positions, for the typical 2009 August 12 a reconstruction. The solid line corresponds to the 1σ confidence level, and the dashed line is the best-fitting error ellipse.

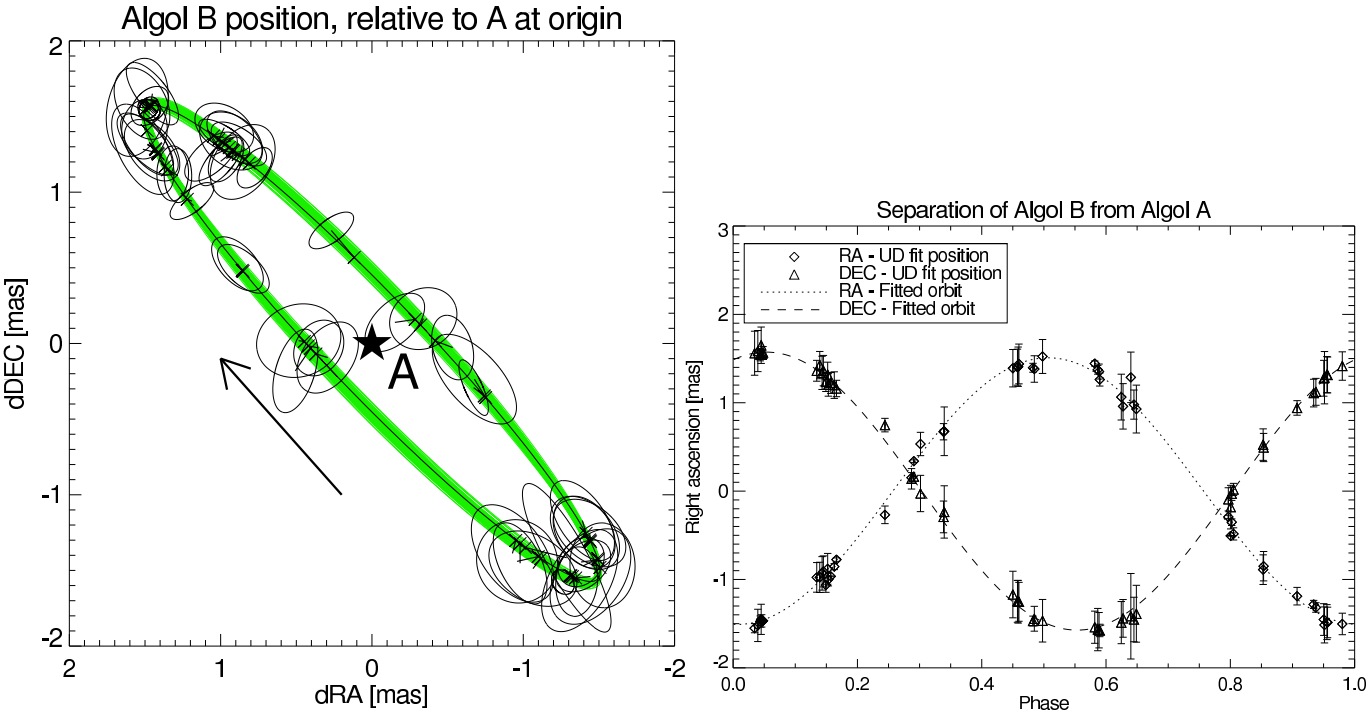

Figure 6. Orbit of the inner binary: (left) band of allowed orbits at 3σ for Algol B relative to Algol A (green), and best fit solution (solid black line) ; the error ellipses for each epoch are derived from the χ^2 distribution maps obtained when fitting a uniform brightness model; (right) declination and right ascension as a function of the inner orbit phase, the zero phase corresponding to the light minima.

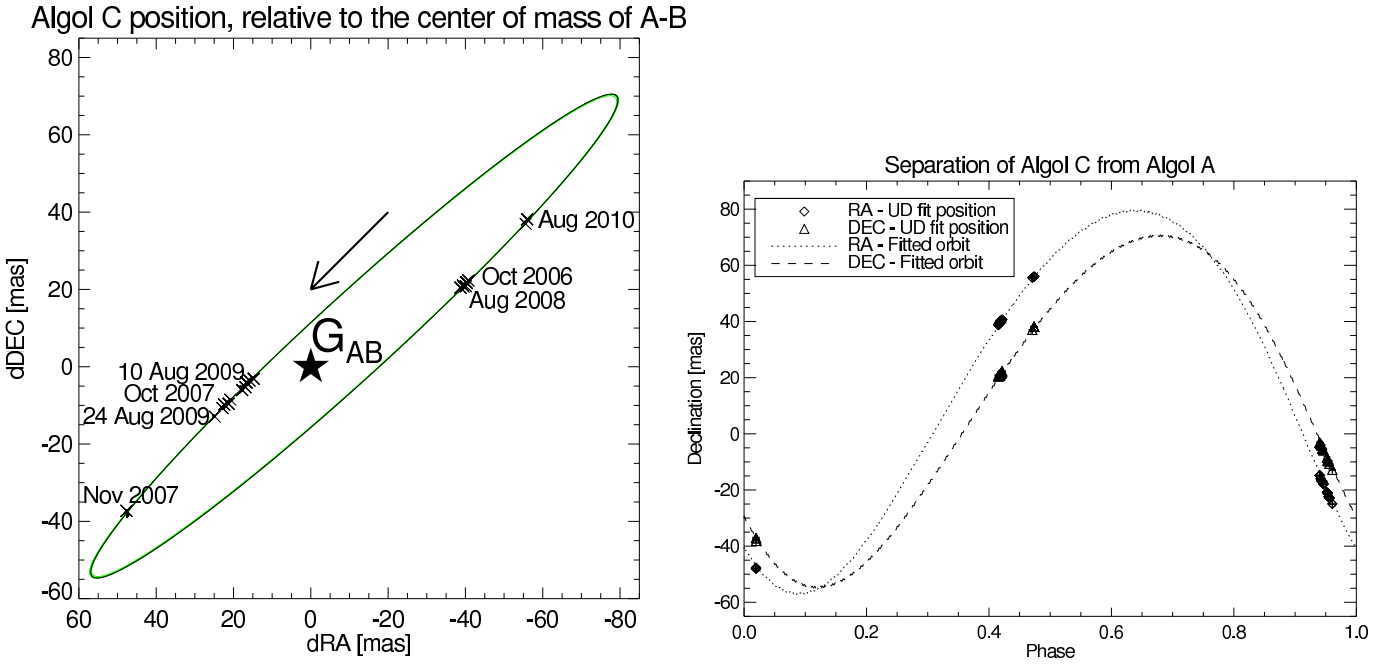

Figure 7. Orbit of the outer binary: (left) band of allowed orbits at 3-σ for Algol C relative to the center of mass of the inner binary A+B (green), and best fit solution (solid black line); (right) declination and right ascension as a function of the outer orbit phase (the reference zero phase is at T_0 given in Table 5); the semi-major axes of the error ellipses are at worse 0.5 mas and thus barely visible.

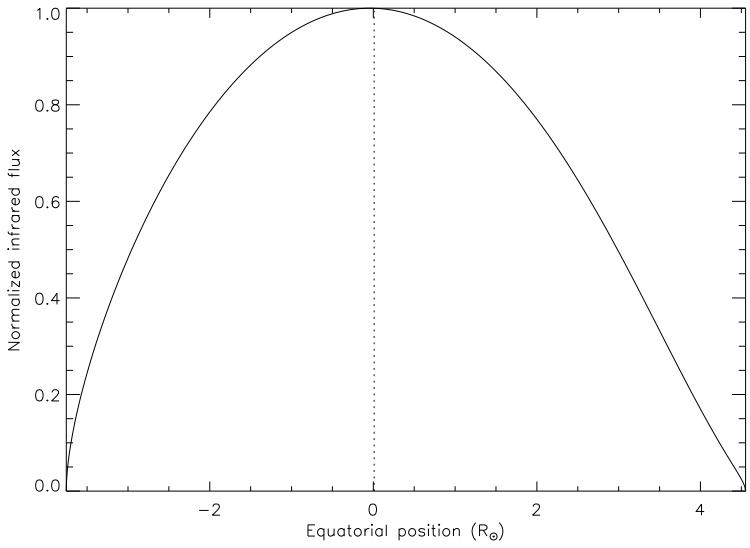

Figure 8. Simulated profile of the equatorial brightness of Algol B for a Roche lobe filling factor of 1.0. As the surface departs from sphericity, the radius-dependent gravity darkening effect induce a shift of the photocenter (dashed line) with respect to the center of mass (zero position). For this simulation, as we move along the equator, we compute the distance of the surface to the center of mass, using the Roche-von Zeipel equation. We then derive the corresponding local gravity and local temperature values. The brightness distribution is given as the combination of gravity darkening and limb darkening. We used the results from infrared light-curve fitting published in Richards (1990) to set the gravity darkening coefficient ($\beta = 0.08$, corresponding to the theoretical result for a convective envelope) and the quadratic limb-darkening coefficients ($u_1 = 0.680$, $u_2 = -0.171$). The reported brightness distribution is normalized to its maximum value. Overall we find that the position of the center of light differs from that of the center of mass by only 1%.

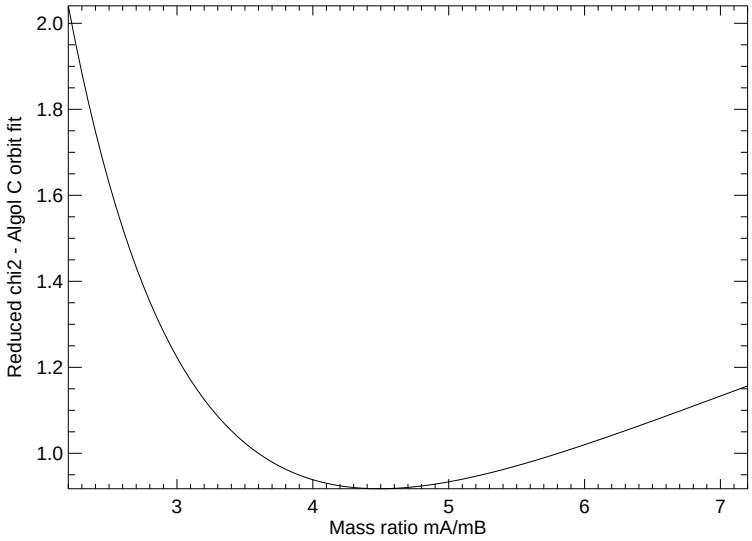

Figure 9. Reduced χ^2 of the best fit of Algol C orbit as a function of the inner pair mass ratio, with a minimum at $m_A/m_B = 4.56 \pm 0.34$.

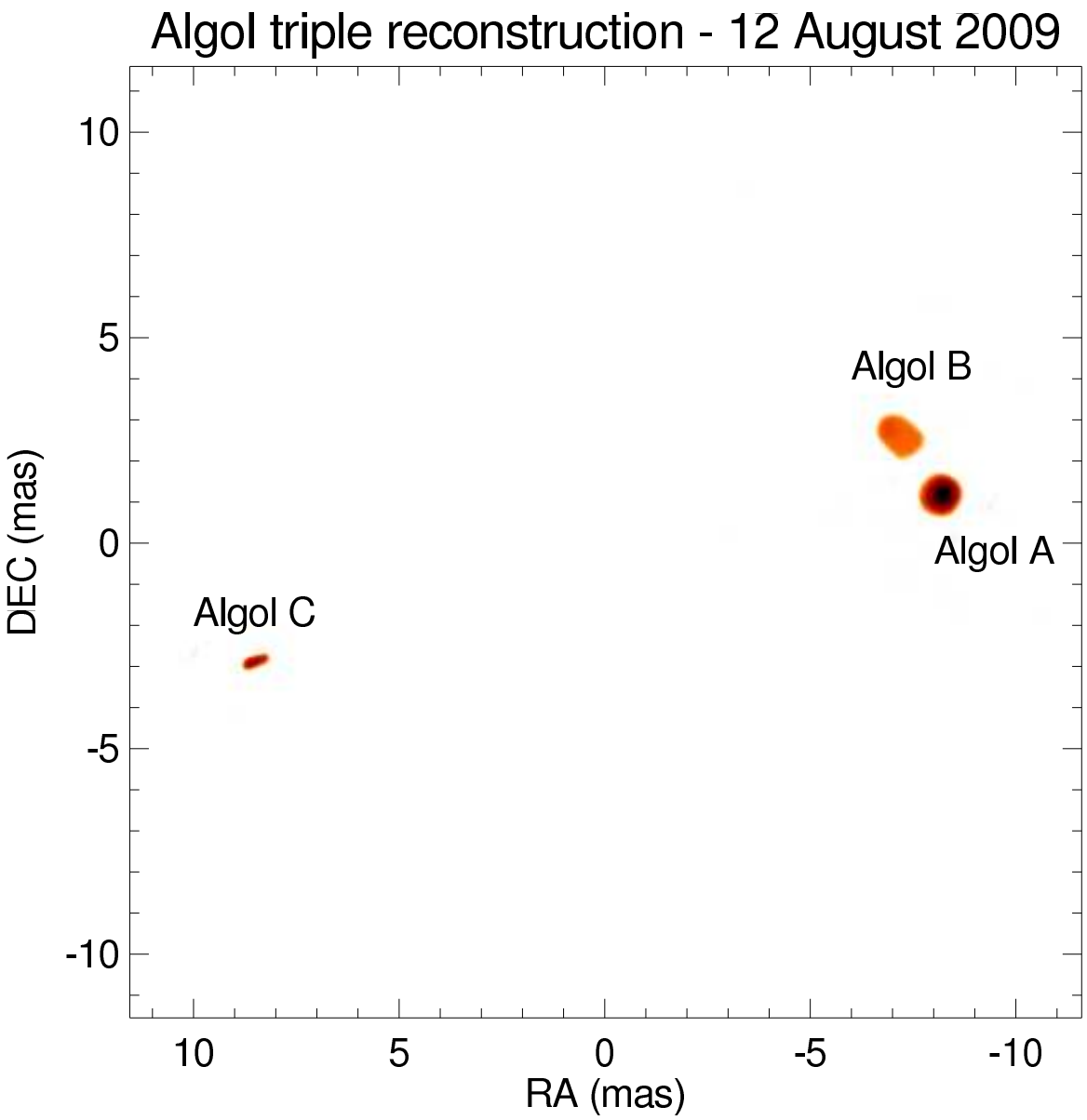

Figure 10. Reconstructed image of the triple system for the 2009 August 12 a data set (final reduced χ^2=1.02). The three components are resolved: Algol A is nearly circular, Algol B is elongated as it fills its Roche lobe, and Algol C is elongated due to bandwidth smearing.

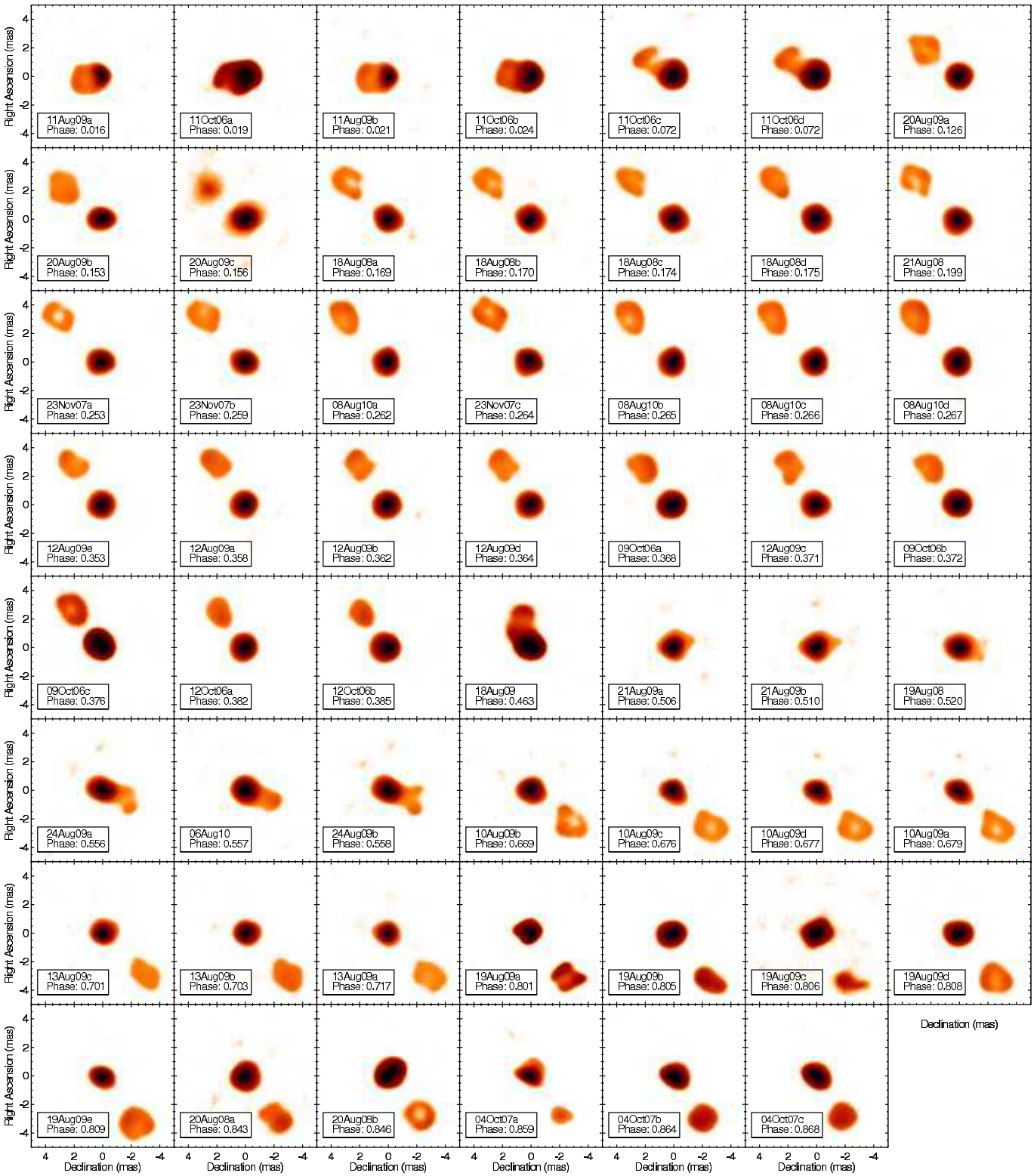

Figure 11. Evolution of the SQUEEZE reconstructions of the inner stellar system A–B with the phase of the primary eclipse. The phase is given as $\Phi = [(T_0 - \mathrm{MJD})/P_{\mathrm{AB}} \mod 1]$ with the orbital elements from Table 6; $\Phi = 0$ corresponds to the primary eclipse and the time of the light minima, and $\Phi = 0.5$ corresponds to the secondary eclipse.

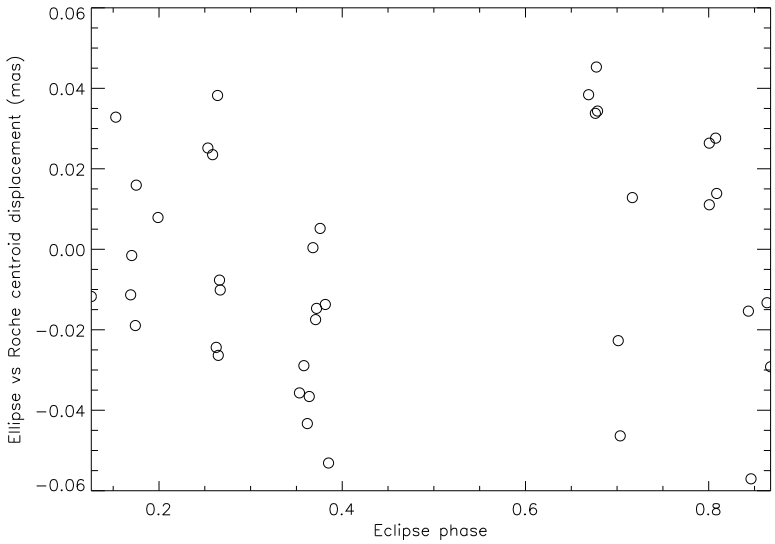

Figure 12. Difference between the principal axis of the inner pair estimated from the reconstructed images and estimated from uniform ellipse model-fitting, as a function of the inner orbit phase. The principal axis was defined as the vector joining the centers of light of Algol A and Algol B, Its computation was restricted to epochs where the stellar disks do not overlap.

Table 3
Position estimates of Algol B and Algol C relative to Algol A

Observation (UT date)	MJD (days)	χ^2/dof	ρ_B (mas)	θ_B (deg)	$\sigma_{a,B}$ (mas)	$\sigma_{b,B}$ (mas)	ψ_B (mas)	ρ_C (mas)	θ_C (deg)	$\sigma_{a,C}$ (mas)	$\sigma_{b,C}$ (mas)	ψ_C (deg)
2006 Oct 9 a	54017.535773	1.452	1.630	40.74	0.214	0.103	318.16	44.54	–61.91	0.217	0.140	302.82
2006 Oct 9 b	54017.547162	1.193	1.565	39.72	0.199	0.083	310.04	44.55	–61.93	0.192	0.141	299.08
2006 Oct 9 c	54017.558304	2.778	1.558	38.24	0.170	0.094	299.65	44.52	–61.88	0.229	0.158	106.26
2006 Oct 11 a	54019.403382	6.467	0.538	109.70	0.286	0.129	286.92	45.09	–61.73	0.331	0.202	108.53
2006 Oct 11 b	54019.416411	4.271	0.485	87.79	0.283	0.238	160.59	45.62	–61.73	0.421	0.179	305.31
2006 Oct 11 c	54019.553074	3.673	1.033	59.38	0.217	0.118	227.40	45.74	–61.66	0.243	0.139	119.75
2006 Oct 11 d	54019.555134	3.188	0.983	59.86	0.211	0.103	222.20	45.88	–61.72	0.234	0.150	298.48
2006 Oct 12 a	54020.441845	1.124	1.473	35.46	0.271	0.183	303.77	46.37	–61.28	0.309	0.184	128.15
2006 Oct 12 b	54020.451949	1.540	1.396	33.72	0.155	0.086	307.40	46.35	–61.31	0.238	0.153	136.16
2007 Oct 4 a	54377.358738	2.891	1.914	–137.73	0.555	0.134	61.12	18.86	108.01	0.374	0.075	67.59
2007 Oct 4 b	54377.372951	2.098	1.752	–146.02	0.289	0.139	64.24	18.81	107.87	0.330	0.100	242.73
2007 Oct 4 c	54377.384093	2.076	1.670	–146.21	0.367	0.207	234.45	18.69	108.25	0.806	0.137	64.15
2007 Nov 23 a	54427.234904	3.484	2.200	44.83	0.330	0.195	103.13	61.06	128.69	0.508	0.157	124.32
2007 Nov 23 b	54427.249729	1.975	2.196	43.80	0.252	0.159	242.64	60.69	127.74	0.449	0.149	125.02
2007 Nov 23 c	54427.265206	2.795	2.198	41.31	0.248	0.100	232.43	60.74	127.75	0.254	0.150	309.56
2008 Aug 18 a	54696.522101	5.493	1.935	48.69	0.234	0.139	231.63	44.17	–62.15	0.344	0.109	298.54
2008 Aug 18 b	54696.525448	3.876	1.985	49.72	0.326	0.158	242.68	43.80	–62.15	0.405	0.178	301.15
2008 Aug 18 c	54696.536763	4.791	1.984	48.36	0.262	0.115	226.02	43.99	–62.12	0.427	0.121	293.89
2008 Aug 18 d	54696.539548	3.268	1.984	48.52	0.243	0.110	231.84	43.83	–62.15	0.401	0.121	296.55
2008 Aug 19	54697.529045	3.965	0.534	–92.89	0.219	0.130	253.86	44.67	–62.38	0.303	0.122	116.32
2008 Aug 20 a	54698.455342	4.235	1.829	–144.44	0.318	0.214	212.86	44.90	–62.52	0.448	0.174	128.07
2008 Aug 20 b	54698.463525	1.703	1.730	–146.33	0.278	0.264	62.05	45.32	–62.46	0.471	0.151	127.81
2008 Aug 21	54699.475045	3.292	2.065	46.72	0.196	0.149	273.80	45.59	–61.46	0.299	0.086	305.89
2009 Aug 10 a	55053.531881	4.257	1.908	–131.04	0.276	0.175	220.41	15.17	102.16	0.320	0.186	131.00
2009 Aug 10 b	55053.503913	3.033	1.818	–130.08	0.302	0.153	235.73	15.15	102.10	0.223	0.177	318.71
2009 Aug 10 c	55053.525093	4.020	1.877	–131.65	0.258	0.179	237.61	15.16	102.12	0.315	0.180	122.35
2009 Aug 10 d	55053.528275	4.348	1.884	–131.65	0.279	0.182	229.05	15.17	102.12	0.325	0.172	130.78
2009 Aug 11 a	55054.497896	3.595	0.307	107.63	0.261	0.167	124.70	16.35	102.97	0.269	0.194	118.47
2009 Aug 11 b	55054.513533	7.212	0.353	94.87	0.194	0.153	121.59	16.38	102.91	0.208	0.148	310.20
2009 Aug 12 a	55055.480222	1.157	1.728	34.39	0.210	0.141	211.54	17.18	103.62	0.124	0.053	300.49
2009 Aug 12 b	55055.490959	0.724	1.630	34.83	0.231	0.163	217.99	17.18	103.68	0.191	0.155	115.96
2009 Aug 12 c	55055.516855	1.169	1.585	33.70	0.211	0.100	214.40	17.20	103.76	0.114	0.091	289.18
2009 Aug 12 d	55055.497004	0.983	1.639	33.68	0.219	0.123	222.33	17.19	103.69	0.099	0.093	332.47
2009 Aug 12 e	55055.466371	0.578	1.676	35.63	0.194	0.071	32.54	17.19	103.65	0.115	0.062	123.01
2009 Aug 13 a	55056.508177	3.446	2.115	–133.91	0.279	0.215	267.54	17.79	107.45	0.266	0.188	122.84
2009 Aug 13 b	55056.470177	2.552	1.999	–136.27	0.175	0.138	–51.76	17.71	107.21	0.181	0.103	299.71
2009 Aug 13 c	55056.463975	1.953	2.027	–136.49	0.207	0.137	140.28	17.77	107.42	0.153	0.099	137.45
2009 Aug 18	55061.515703	2.238	0.794	19.77	0.175	0.076	143.17	22.44	112.29	0.360	0.062	246.93
2009 Aug 19 a	55062.483659	5.451	2.111	–136.85	0.349	0.219	124.05	23.14	114.34	0.432	0.179	126.58
2009 Aug 19 b	55062.497488	2.599	2.083	–138.78	0.369	0.200	119.47	23.21	114.27	0.336	0.195	129.47
2009 Aug 19 d	55062.503528	3.903	2.076	–139.32	0.229	0.137	275.62	23.29	114.34	0.190	0.114	302.48
2009 Aug 19 e	55062.506739	7.770	2.020	–141.33	0.087	0.068	54.47	23.22	114.25	0.099	0.061	122.80
2009 Aug 20 a	55063.416862	2.399	1.516	51.64	0.174	0.072	141.62	24.38	113.59	0.195	0.129	101.55
2009 Aug 20 b	55063.493563	1.571	1.696	49.13	0.178	0.090	89.27	24.44	113.54	0.191	0.118	239.39
2009 Aug 20 c	55063.503760	1.862	1.731	49.53	0.182	0.104	90.96	24.44	113.48	0.180	0.162	68.83
2009 Aug 21 a	55064.505563	2.316	0.206	–47.38	0.240	0.134	316.11	25.26	115.08	0.183	0.142	106.54
2009 Aug 21 b	55064.516370	4.145	0.377	–64.16	0.231	0.195	330.11	25.26	115.07	0.171	0.131	199.17
2009 Aug 24 b	55067.523787	8.119	0.717	–109.20	0.367	0.175	227.88	28.05	117.26	0.285	0.262	291.42
2010 Aug 6	55414.467228	1.507	0.733	–113.48	0.199	0.059	65.96	66.78	–56.36	0.260	0.085	133.57
2010 Aug 8 a	55416.489153	0.693	2.135	43.70	0.079	0.062	403.26	67.73	–55.73	0.139	0.053	128.93
2010 Aug 8 b	55416.495590	0.737	2.130	43.59	0.068	0.073	64.08	67.73	–55.74	0.111	0.050	126.83
2010 Aug 8 c	55416.499486	0.821	2.144	43.41	0.076	0.060	120.88	67.69	–55.75	0.137	0.047	125.75
2010 Aug 8 d	55416.501757	0.628	2.149	43.08	0.149	0.100	312.13	67.72	–55.75	0.222	0.079	132.75

Note. — All angles are given east of north. ρ_B and θ_B are the polar coordinates of Algol B, while $\sigma_{a,B}$, $\sigma_{b,B}$, and ψ_B are, respectively, the semimajor axis, semiminor axis, and angular inclination of its error ellipse.

Table 4
Radius and Mass Estimates of Algol A, Algol B and Algol C.

	Richards et al. (1993)	Zavala et al. (2010)	This Work[a]
R_A ($R_\odot$)	2.90 ± 0.04	...	2.73 ± 0.20
R_B ($R_\odot$)	3.5 ± 0.1	...	3.48 ± 0.28
R_C ($R_\odot$)	1.7	...	1.73 ± 0.33
M_A ($M_\odot$)	3.7 ± 0.3	3.7 ± 0.2[b]	3.17 ± 0.21
M_B ($M_\odot$)	0.81 ± 0.05	0.8 ± 0.1[b]	0.70 ± 0.08
M_C ($M_\odot$)	1.6 ± 0.1	1.5 ± 0.1[b]	1.76 ± 0.15

[a] Assuming a parallax of 34.7 ± 0.6 mas (Zavala et al. 2010; Peterson et al. 2011).
[b] Initially based on Richards (1993), then re-optimized using the Navy Optical Interferometer data.

Table 5
Orbital Parameters for the Outer Orbit.

Orbital Element	Zavala et al. (2010)	This Work
T_0 (JD)	2446931.6 ± 0.1	$2446927.22^{+0.60}_{-0.54}$
P (days)	679.85 ± 0.04	680.168 ± 0.046
a (mas)	93.8 ± 0.2	$93.43^{+0.12}_{-0.09}$
i (deg)	83.7 ± 0.1	83.66 ± 0.03
Ω (deg)	132.7 ± 0.1	132.66 ± 0.08
e	0.225 ± 0.005	0.227 ± 0.002
ω (deg)	310.8 ± 0.1	310.02 ± 0.26
m_A/m_B	...	4.56 ± 0.34
$mC/(mA + mB)$	...	0.456 ± 0.022

Table 6
Orbital Parameters for the Inner Orbit

Orbital Element	Zavala et al. (2010)	This work
T_0 (JD) [a]	2441771.3395	2441771.353 ± 0.007
P (days)	2.867328	$2.867328 \pm 5 \times 10^{-5}$
a (mas)	2.3 ± 0.1	2.15 ± 0.05
i (deg)	98.6	98.70 ± 0.65
Ω (deg)	47.4 ± 5.2	43.43 ± 0.32
e	0	0
ω (deg)	...	...

[a] Time of minimum light at the primary eclipse.